

Non-Linear Phase-Retrieval Algorithms for X-ray Propagation-Based Phase-Contrast Tomography

K. Aditya Mohan¹, Senior Member, IEEE, Jean-Baptiste Forien¹, Venkatesh Sridhar¹, Member, IEEE, Jefferson Cuadra, Dilworth Parkinson¹, Member, IEEE

Abstract—X-ray phase-contrast tomography (XPCT) is widely used for high-contrast 3D micron-scale imaging using nearly monochromatic X-rays at synchrotron beamlines. XPCT enables an order of magnitude improvement in image contrast of the reconstructed material interfaces with low X-ray absorption contrast. The dominant approaches to 3D reconstruction using XPCT relies on the use of phase-retrieval algorithms that make one or more limiting approximations for the experimental configuration and material properties. Since many experimental scenarios violate such approximations, the resulting reconstructions contain blur, artifacts, or other quantitative inaccuracies. Our solution to this problem is to formulate new iterative non-linear phase-retrieval (NLPR) algorithms that avoid such limiting approximations. Compared to the widely used state-of-the-art approaches, we show that our proposed algorithms result in sharp and quantitatively accurate reconstruction with reduced artifacts. Unlike existing NLPR algorithms, our approaches avoid the laborious manual tuning of regularization hyper-parameters while still achieving the stated goals. As an alternative to regularization, we propose explicit constraints on the material properties to constrain the solution space and solve the phase-retrieval problem. These constraints are easily user-configurable since they follow directly from the imaged object's dimensions and material properties.

Index Terms—Phase-retrieval, phase-contrast, X-ray, CT, reconstruction, tomography, synchrotron.

I. INTRODUCTION

Propagation-based X-ray Phase-Contrast Tomography (XPCT) at synchrotron beamlines is widely used for 3D imaging due to the high-intensity, monochromatic, spatially coherent, and parallel-beam properties of synchrotron X-rays. XPCT is used for 3D reconstruction of a wide variety of objects in biology [1], [2], material science [3]–[6], medical imaging [7], [8], and paleontology [9], [10]. In synchrotron XPCT¹, the object is exposed to a parallel beam of X-rays and the X-ray intensity is recorded by a 2D detector at several rotation angles of the object (Fig. 1). The magnitude of phase-contrast in the X-ray images is dependent on the propagation distance between the imaged object and the detector. The propagation distance is adjusted to be sufficiently large to achieve adequate phase-contrast in the X-ray images. XPCT can either be performed at a single object-to-detector distance or be repeated at several object-to-detector distances.

K. A. Mohan, J. B. Forien, and V. Sridhar are affiliated with Lawrence Livermore National Laboratory, Livermore, CA. D. Parkinson is affiliated with Lawrence Berkeley National Laboratory, Berkeley, CA. J. Cuadra's contributions to this paper was made when he was affiliated with Lawrence Livermore National Laboratory, Livermore, CA.

¹Henceforth, XPCT refers to XPCT using the monochromatic, parallel, and coherent X-rays at a synchrotron.

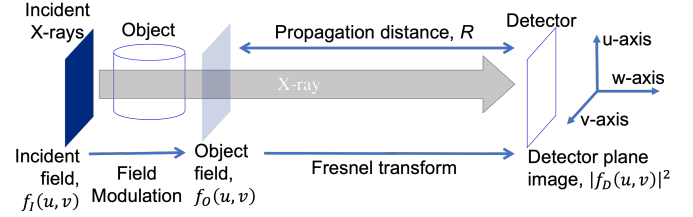


Fig. 1. Parallel-beam X-ray phase-contrast tomography (XPCT) experiment at a synchrotron user-facility. The 3D object is rotated along an axis and 2D detector measurements are periodically acquired at several rotation angles. The object-to-detector propagation distance, R , needs to be sufficiently large to produce phase-contrast in the measured X-ray images. The labels for the X-ray fields are defined in section II.

The solution to the inverse problem of object reconstruction is a combination of two sequentially steps. First, we perform 2D phase-retrieval at each tomographic view to reconstruct images of the transmitted field, $f_O(u, v)$ in Fig. 1, or its phase-shift from the detector images $|f_D(u, v)|^2$ [11], [12]. Henceforth, we shall refer to the phase component of the recovered field $f_O(u, v)$ as the phase image. Next, we use a tomographic reconstruction algorithm to reconstruct the 3D refractive index decrement of the object from the phase images [13]. During phase-retrieval, the goal is to reconstruct the 2D phase image at each tomographic view from X-ray images at one or more propagation distances. Phase retrieval is a non-linear inverse problem since it relies on the inversion of a non-linear analytical forward model that relates the phase to the X-ray images. The tomographic reconstruction step is used to reconstruct the 3D refractive index decrement from the retrieved phase images at all the views. Reconstruction of the refractive index decrement from the phase images is a linear inverse problem that is solved using any analytical or iterative CT reconstruction method, including the widely used filtered back projection (FBP) algorithm [13].

The popular choice for phase-retrieval algorithms in XPCT relies on the inversion of forward models that express the measured X-ray images² as a linear transformation of the phase image. For XPCT using X-ray images at a single propagation distance, phase-retrieval reduces to the application of a digital linear filter on the individual X-ray images [11], [14]–[18]. These methods also constrain the material composition by approximating the absorption index to be zero or enforcing a proportionality relation between the refractive index decrement

²Or, simple functional forms such as affine and/or logarithm transforms of the X-ray images are expressed as a linear transform of the phase.

and the absorption index. In the case of multi-distance XPCT, phase-retrieval is performed by the inversion of approximate linear relations between the multi-distance X-ray images and the phase [12], [19]–[23]. Some of these methods do not constrain the material composition by avoiding the approximations of zero-absorption and phase-absorption proportionality [12], [19], [20]. While such linear phase retrieval (LPR) algorithms are computationally fast, the forward modeling approximations severely restrict the material composition and experimental design. If LPR algorithms are used outside their range of validity, they produce reconstructions with quantitative inaccuracies, false (unwanted) artifacts, and/or image blur.

To address the limitations of linear phase retrieval (LPR), several non-linear phase-retrieval (NLPR) algorithms have been proposed that avoid the linear approximations made in the forward measurement model [24]–[28]. NLPR estimates the phase images such that it minimizes a measure of the distance between the X-ray images and the output of a non-linear forward measurement model under certain regularizing constraints. The non-linear forward model uses the Fresnel propagator to express the X-ray intensity at the detector as a function of the phase-shift in the plane immediately downstream of the object (also called the exit plane). Existing NLPR algorithms [24]–[28] use regularization functions to enforce sparsity constraints and limit the solution space for the X-ray phase images. However, these approaches require the user to manually tune one or more regularization parameters to achieve the claimed performance improvements of artifact reduction, improved sharpness, and quantitative accuracy. The high complexity of computational implementation along with the absence of user-friendly open-source software implementations have further prevented widespread use of these methods.

In recent years, several deep learning (DL) approaches [29]–[34] have also been proposed for phase-retrieval in XPCT. Using DL, the authors demonstrated improved performance without the excessive computational cost of NLPR approaches. However, DL approaches rely on data for training the neural which limits the range-of-applicability to objects that are representative of the trained data. Importantly, collection of high-fidelity representative data using XPCT experiments may be infeasible. In contrast, both LPR and NLPR algorithms do not require any training data and are broadly applicable to a wide range of objects.

In this paper, we present new non-linear phase-retrieval (NLPR) algorithms for both single-distance and multi-distance XPCT. A limited version of this manuscript with preliminary results was published in the form of a conference proceedings paper [35]. Our NLPR algorithms also support constraints on the material composition. In particular, we demonstrate the use of the phase-absorption proportionality constraint for single-distance XPCT. First, we formulate discrete non-linear forward models using the Fresnel transform in Fourier frequency space. This model expresses the measured data as an analytical non-linear function of the phase images. Next, we formulate an objective function that is a measure of the distance between the measured data and the forward model output. Unlike existing non-linear approaches, we do not use prior-models or regularization functions in the objective

function to achieve the desired goals of artifact-free, sharp, and accurate reconstructions. Finally, we iteratively solve for the phase images that minimize the objective function while also satisfying any constraint on the material composition. We have released our phase-retrieval software under an open-source license along with documentation at the link <https://github.com/PhaseTorch/PhaseTorch>.

We implemented our algorithms using the *PyTorch* framework and python programming language. For faster computation, our algorithms can also be run on multiple GPUs. The characteristics of our NLPR algorithms are listed below -

- Quantitatively accurate and sharp reconstructions with reduced artifacts compared to LPR approaches.
- Avoids manual tuning of regularization hyper-parameters due to the absence of regularizing prior models.
- Optional constraints such as homogeneous object, phase-absorption proportionality, or zero-absorption.
- Open-source software with documentation.

II. X-RAY MEASUREMENT PHYSICS

In this section, we present a mathematical formulation for the physics of measurement in XPCT.

A. Modulation of the X-ray Field

In XPCT, the measured data is sensitive to the 3D variations in the absorption index, $\beta(u, v, w)$, and refractive index decrement, $\delta(u, v, w)$, of the imaged object. Here, (u, v, w) represents the 3D Cartesian coordinate system such that the X-ray propagation is along the w -axis and perpendicular to the $u - v$ plane. The absorption index and refractive index decrement are expressed compactly as the complex refractive index $n(u, v, w) = 1 - \delta(u, v, w) + i\beta(u, v, w)$.

As X-rays propagate through an object, the X-ray field undergoes a change in both amplitude and phase. The reduction in X-ray intensity after propagation through an object is a direct measure of the object's absorption index, $\beta(u, v, w)$. Alternatively, the phase shift of the X-ray field that is induced by the object is a direct measure of its refractive index decrement, $\delta(u, v, w)$. Ignoring constant phase terms, the modulated X-ray field, $f_O(u, v)$, is expressed as,

$$f_O(u, v) = f_I(u, v)T(u, v), \quad (1)$$

where $T(u, v)$ is the transmission function such that $T(u, v) = \exp\{-A(u, v) - i\phi(u, v)\}$, where

$$A(u, v) = \frac{2\pi}{\lambda} \int_w \beta(u, v, w) dw \text{ and } \phi(u, v) = \frac{2\pi}{\lambda} \int_w \delta(u, v, w) dw. \quad (2)$$

Here, λ is the wavelength of the monochromatic and coherent X-ray field.

B. Measurement of Fresnel Propagated Field

As the X-ray field propagates from the object to the detector, the phase shifts induced by the object manifest as Fresnel diffraction fringes in the X-ray intensity images

that are measured at the detector. The X-ray field at the detector plane, $f_D(u, v)$, is expressed as a 2D convolution of the X-ray field at the exit plane, $f_O(u, v)$, downstream of the sample and the Fresnel impulse response function, $\exp\{(i\pi)/(\lambda R)(u^2 + v^2)\}$, where R is the object to detector distance [12], [24], [35]. The X-ray field propagation is depicted in Fig. 1.

Fresnel transform is more efficiently computed in Fourier frequency space. Let $F_D(\mu, \nu)$ and $F_O(\mu, \nu)$ denote the 2D Fourier transform of the X-ray fields $f_D(u, v)$ and $f_O(u, v)$ respectively, where (μ, ν) are the 2D Fourier frequency coordinates. Then,

$$F_D(\mu, \nu) = F_O(\mu, \nu) \exp\{-i\pi\lambda R(\mu^2 + \nu^2)\}. \quad (3)$$

Information on the phase of the X-ray field is lost since detector measurements are only sensitive to the intensity of the X-ray field. Thus, the detector measurements are modeled as,

$$\tilde{y}(j, k) = |f_D(j\Delta, k\Delta)|^2, \quad (4)$$

where Δ is the width of each detector pixel and $|\cdot|$ denotes the magnitude of a complex number.

C. Data Normalization

Bright-field (a.k.a. flat-field) and dark-field measurements are acquired to appropriately normalize the CT scans. Bright-field refers to measurements made with the X-ray beam but without the object and dark-field refers to measurements made in the absence of the X-ray beam. Typically, bright-field and dark-field measurements are made at the same propagation distances as required for the phase-contrast CT scans. Since this data is at the detector position optimized for phase-contrast, it is insufficient to estimate the phase and amplitude of the incident X-ray field $f_I(u, v)$.

For normalization, we make certain simplifying approximations on $f_I(u, v)$ that also serve to simplify the subsequent problem of phase-retrieval. First, we approximate the incident field $f_I(u, v)$ as a plane wave with constant phase. Without loss of generality, we assume that this constant phase is zero since any information on constant phase terms is lost (equation (4)). Next, we normalize the detector measurements $\tilde{y}(j, k)$ using the bright- and dark-fields. This normalization enables us to model the incident field $f_I(u, v)$ as having unit amplitude. Lastly, we compute the square root of the normalized detector image before running the algorithms presented in section IV. Let $b(j, k)$ and $d(j, k)$ denote the bright-field and dark-field measurements respectively for the phase-contrast image $\tilde{y}(j, k)$. Then, the square root of the normalized detector image is given by,

$$y(j, k) = \sqrt{\frac{\tilde{y}(j, k) - d(j, k)}{b(j, k) - d(j, k)}}. \quad (5)$$

III. FORWARD MODEL

The forward models formulated in this section will be used in the phase-retrieval algorithms that estimate the transmission function from the measurements $\tilde{y}(j, k)$. To formulate a forward model, we first translate the continuous space expressions

in section II to discrete space. Let $x(j, k)$ denote a sampling of the transmission function $T(u, v)$ in equation (1). Let $g_D(j, k)$, $g_O(j, k)$, and $g_I(j, k)$ denote the sampled discrete representation of the continuous space X-ray fields $f_D(u, v)$, $f_O(u, v)$, and $f_I(u, v)$ respectively³. Let $G_D(p, q)$, $G_O(p, q)$, and $G_I(p, q)$ represent the discrete Fourier transform (DFT) coefficients of $g_D(j, k)$, $g_O(j, k)$, and $g_I(j, k)$ respectively.

A. Discretization of Measurement Model

We derive the discretized relation between the incident X-ray field $g_I(j, k)$ and the X-ray field $g_O(j, k)$ at the exit plane of the object. Given that $x(j, k)$ represents the transmission function in discrete space, we have,

$$g_O(j, k) = g_I(j, k)x(j, k). \quad (6)$$

Next, we discretize the relation between the detector measurements $y(j, k)$ in equation (5) and the X-ray field $g_O(j, k)$ at the exit plane of the object. To sample the Fresnel transform in equation (3), we substitute $\mu = p\Delta_\mu$ and $\nu = q\Delta_\nu$, where (p, q) are the discrete frequency coordinates, $\Delta_\mu = \frac{1}{N_u\Delta}$ is the sampling width along the μ -axis, and $\Delta_\nu = \frac{1}{N_v\Delta}$ is the sampling width along the ν -axis. Note that N_u and N_v are the number of discrete coordinates along the u -axis and v -axis respectively. Thus, a discrete sampling of Fourier space Fresnel transform is given by,

$$H(p, q) = \exp\{-i\pi\lambda R(p^2\Delta_\mu^2 + q^2\Delta_\nu^2)\}. \quad (7)$$

Given equation (7), we can now express the relation between the DFT $G_D(p, q)$ of $g_D(i, j)$ and DFT $G_O(p, q)$ of $g_O(i, j)$ as,

$$G_D(p, q) = H(p, q)G_O(p, q). \quad (8)$$

We use edge padding in the space domain for $g_O(j, k)$ to avoid circular convolution artifacts. Since the detector only measures the intensity of the X-ray field, the square root of the detector measurement is expressed as,

$$y(j, k) = |g_D(j, k)|, \quad (9)$$

where $g_D(j, k)$ is the discrete X-ray field in the detector plane given by the inverse discrete Fourier transform (IDFT) of $G_D(p, q)$ and $|\cdot|$ denotes the magnitude of a complex number.

In practice, the noise in detector measurements is modeled using Poisson statistics. Due to the variance stabilizing property of the square root transformation of Poisson random variables [36], we can model the noise statistics of the square root detector measurement $y(j, k)$ in equation (5) as a Gaussian distribution with constant variance. Thus, the forward model for the square root detector measurement is given by,

$$y(j, k) = |g_D(j, k)| + n(j, k), \quad (10)$$

where $n(j, k)$ is additive Gaussian noise with a constant variance for all j and k .

³ $g_D(j, k)$, $g_O(j, k)$, and $g_I(j, k)$ are a sampling of the X-ray fields $f_D(u, v)$, $f_O(u, v)$, and $f_I(u, v)$ in discrete space such that $u = j\Delta$ and $v = k\Delta$.

B. Non-Linear Forward Models for XPCT

The forward model that relates $y(j, k)$ to $x(j, k)$ is obtained by combining equations (6), (8), and (10). For convenience of notation, we will use matrix-vector notation for mathematical formulation of the forward model in discrete space. In section III-B1, we present a forward model where $x(j, k)$ is unconstrained, which does not impose restrictions on the material composition of the imaged object. In this case, the $x(j, k)$ is a complex valued number that uniquely encodes the X-ray phase-shift and total X-ray absorption by the object. In section III-B2, we present a forward model where $x(j, k)$ is constrained, which restricts the material composition of the imaged object. In this case, the feasible solution space of the complex valued $x(j, k)$ is restricted such that it can only be expressed as the function of a real valued $z(j, k)$. This constraint is useful to restrict the feasible solution space for the phase-shift and X-ray absorption.

1) *Unconstrained \mathbf{x}* : Let \mathbf{y} , \mathbf{x} , and \mathbf{n} be column vectors whose elements include a raster ordering of the discrete samples $y(j, k)$, $x(j, k)$, and $n(j, k)$ respectively. The matrix \mathbf{H} is an operator that when left-multiplied to \mathbf{x} returns the Fresnel transform of \mathbf{x} . The forward model computes the magnitude of the IDFT of the Fresnel transform (equation (8)) of the DFT of $x(j, k)$. The vector form of the unconstrained forward model is,

$$\mathbf{y} = |\mathbf{H}\mathbf{x}| + \mathbf{n}. \quad (11)$$

where $|\cdot|$ denotes element-wise magnitude. The DFT and IDFT operations are implemented using fast Fourier transform algorithms. Equation (11) expresses the dependence of the real valued measurement vector \mathbf{y} on the complex valued transmission vector \mathbf{x} .

2) *Constrained \mathbf{x}* : In the absence of data \mathbf{y} at multiple propagation distances, unique reconstruction of \mathbf{x} is achieved only by imposing constraints on the imaged sample. For single-distance XPCT, it is typical to use constraints such as single material [14], phase-absorption proportionality [18], or zero absorption [17]. However, such constraints may introduce inaccuracies and artifacts for objects that do not satisfy these constraints.

The single-material and phase-absorption proportionality constraints are mathematically expressed as,

$$\delta(u, v, w) \propto \beta(u, v, w) \Rightarrow \phi(u, v) \propto A(u, v). \quad (12)$$

Alternatively, under the zero-absorption constraint, we have,

$$\beta(u, v, w) = 0 \Rightarrow A(u, v) = 0. \quad (13)$$

The two constraints in equations (12) and (13) are equivalent to expressing the complex valued \mathbf{x} in terms of a real valued \mathbf{z} such that,

$$\mathbf{x} = \mathbf{z}^{\alpha+i\gamma}, \quad (14)$$

where α and γ are real valued constants. For the phase-absorption proportionality constraint (equation (12)), we set the ratio of γ to α equal to the ratio of the refractive index decrement δ to the absorption index β . For the zero-absorption constraint in equation (13), we set $\alpha = 0$. We discuss the

possible choices for α and γ and the associated trade-offs in section IV-B.

Equation (14) halves the dimensionality of the phase retrieval problem by expressing the complex valued vector \mathbf{x} in equation (11) as a function of a real valued vector \mathbf{z} . Given the constraint in equation (14), the forward model that expresses \mathbf{y} in terms of \mathbf{z} is given by,

$$\mathbf{y} = |\mathbf{H}\mathbf{z}^{\alpha+i\gamma}| + \mathbf{n}. \quad (15)$$

IV. NON-LINEAR PHASE RETRIEVAL (NLPR)

In this section, we will formulate phase-retrieval algorithms using the maximum likelihood (ML) estimation framework. The reconstruction \mathbf{x} is such that it minimizes the negative log-likelihood function $l(\mathbf{y}; \mathbf{x})$, which is a measure of the statistical likelihood of the measurement data \mathbf{y} given the transmission function \mathbf{x} . Under the ML framework, we perform phase retrieval by solving the optimization problem of $\hat{\mathbf{x}} = \arg \min_{\mathbf{x}} l(\mathbf{y}; \mathbf{x})$. First, we formulate an approach to estimate the unconstrained transmission function \mathbf{x} . Next, we present an approach to estimate \mathbf{x} such that it also satisfies the constraint in equation (14). Finally, we solve for the X-ray absorption and phase shift at the exit plane of the object from the estimated \mathbf{x} . We do not use a prior likelihood model to enforce sparsity in reconstruction of \mathbf{x} . Instead, we use intelligent initialization for \mathbf{x} from conventional phase-retrieval algorithms, which mimics the role of regularization and leads to improved solutions.

A. Unconstrained NLPR (U-NLPR)

To reconstruct \mathbf{x} without any constraints, we utilize X-ray images at several propagation distances. Importantly, the X-ray images must be registered so that the object appears at the same location in the X-ray images at all the distances. Let \mathbf{y}_l denote the square root detector measurements at a propagation distance of R_l . Then, the negative log-likelihood function is $l(\mathbf{y}; \mathbf{x}) = \frac{1}{\sigma^2} \sum_{l=1}^L \|\mathbf{y}_l - |\mathbf{H}_l \mathbf{x}|\|_2^2$, where L is the total number of distances. Here, the noise in each element of \mathbf{y}_l is approximated to be additive Gaussian with variance σ^2 and $\|\cdot\|_2^2$ denotes the squared l^2 norm of a vector. Thus, the unconstrained \mathbf{x} is estimated by solving the following optimization problem,

$$\hat{\mathbf{x}} = \arg \min_{\mathbf{x}} l(\mathbf{y}; \mathbf{x}) = \arg \min_{\mathbf{x}} \sum_{l=1}^L \|\mathbf{y}_l - |\mathbf{H}_l \mathbf{x}|\|_2^2. \quad (16)$$

We call this approach as unconstrained NLPR (U-NLPR).

The performance of U-NLPR is dependent on the initial estimate for \mathbf{x} that is used to initialize the optimization in equation (16). If the phase and absorption in equation (2) are set to zero, then each element of the vector \mathbf{x} is 1. For multi-distance phase-retrieval using U-NLPR, we show in section VI that zero-initialization for the phase/absorption leads to improved results compared to the state-of-the-art conventional approaches to multi-distance phase-retrieval. However, we also demonstrate that initialization using conventional phase-retrieval methods can further improve the performance of U-NLPR. Unlike U-NLPR, these conventional phase-retrieval

methods use a regularization parameter α' that must be fine-tuned for acceptable performance [12]. The value of this regularization parameter α' will impact both the performance of the conventional phase-retrieval method used for initialization of U-NLPR and the U-NLPR algorithm. To achieve the best performance for U-NLPR without the need for parameter tuning, we use the Contrast Transfer Function (CTF) phase-retrieval [12] with a sufficiently low value for the regularization given by,

$$\alpha' = 2\nu(BC - A^2), \quad (17)$$

where ν is a very small value and the term $(BC - A^2)$ is defined in the reference [12]. In this paper, we set $\nu = 10^{-8}$.

B. Constrained NLPR (C-NLPR)

Using measurements at a single propagation distance, it is not possible to independently reconstruct both the phase and absorption of the X-ray field propagating through the imaged objects. Information on the phase and absorption are entangled in the X-ray intensity measurements. Hence, we impose restrictions on the composition of the object to halve the number of unknowns during phase-retrieval using equation (14).

Let y_l denote the square root detector measurements at a propagation distance of R_l . Then, the negative log-likelihood function is $l(\mathbf{y}; \mathbf{z}) = \frac{1}{\sigma^2} \sum_{l=1}^L \|\mathbf{y}_l - |\mathbf{H}_l \mathbf{z}^{\alpha+i\gamma}|\|_2^2$. We estimate \mathbf{z} by solving the following optimization problem,

$$\hat{\mathbf{z}} = \arg \min_{\mathbf{z}} l(\mathbf{y}; \mathbf{z}) = \arg \min_{\mathbf{z}} \sum_{l=1}^L \|\mathbf{y}_l - |\mathbf{H}_l \mathbf{z}^{\alpha+i\gamma}|\|_2^2. \quad (18)$$

The complex valued transmission function is then estimated as $\hat{\mathbf{x}} = \hat{\mathbf{z}}^{\alpha+i\gamma}$. This method is called constrained NLPR (C-NLPR).

The scalar constraint parameters of α and γ are dependent on the material composition. They also influence the speed of convergence of C-NLPR. Hence, it is important to intelligently set the parameters of α and γ . For a pure-phase object with zero absorption, we can choose $\alpha = 0$ and $\gamma = 1$. However, reconstruction of pure-phase objects will not be investigated in this paper. If a sample is homogeneous, i.e., consists of a single material [14] or satisfies the phase-absorption proportionality constraint [18], then we have several choices for setting α and γ . Let δ and β denote the scalar value of the refractive index decrement and absorption index under these constraints, i.e., assume $\delta(u, v, w)/\beta(u, v, w) = \delta/\beta \forall u, v, w$.

1) *C-NLPR / One- α* : For this constraint, we set $\alpha = 1$ such that $\mathbf{x} = \mathbf{z}^{1+i\gamma}$ from equation (14). From equations (2) and (14), we see that $|\mathbf{x}| = \mathbf{z}$ is a discretization of the absolute value for the transmission function $|T(u, v)| = \exp\{-A(u, v)\}$. The dynamic range of \mathbf{z} is determined by the corresponding dynamic ranges for $A(u, v)$ that is in-turn determined by $\beta(u, v, w)$. For low X-ray absorption materials, if \mathbf{z}_n denotes the n^{th} element of \mathbf{z} , then $\mathbf{z}_n \approx 1$ since $\beta \approx 0$. Hence, $\alpha = 1$ may lead to very slow convergence or numerical instabilities at very low values of β . Since \mathbf{z} is the discretized representation of $\exp\{-A(u, v)\}$, \mathbf{z}^γ is a discretization of $\exp\{-\phi(u, v)\}$ only when $\gamma = \delta/\beta$. Hence, $\alpha = 1$ and

$\gamma = \delta/\beta$ leads to the parameterization of $\mathbf{x} = \mathbf{z}^{1+i\delta/\beta}$, which only requires knowledge of the ratio of δ/β . This method will be referred to as C-NLPR/One- α .

2) *C-NLPR / One- γ* : For this constraint, we set $\gamma = 1$ such that $\mathbf{x} = \mathbf{z}^{\alpha+i}$ from equation (14). From equations (2) and (14), we see that \mathbf{z}^γ is a discretization of the phase component of the transmission function $\exp\{-\phi(u, v)\}$. The dynamic range of \mathbf{z} is determined by the corresponding dynamic range of $\phi(u, v)$ or $\delta(u, v, w)$. For objects with a high refractive index decrement, if \mathbf{z}_n denotes the n^{th} element of \mathbf{z} , then $\mathbf{z}_n \approx 0$ if δ is very large. Hence, $\gamma = 1$ may lead to very slow convergence or numerical instabilities for highly refractive materials. Since \mathbf{z} is a discretization of $\exp\{-\phi(u, v)\}$, \mathbf{z}^α will represent $\exp\{-A(u, v)\}$ only when $\alpha = \beta/\delta$. Hence, $\gamma = 1$ and $\alpha = \beta/\delta$ leads to the parameterization of $\mathbf{x} = \mathbf{z}^{\beta/\delta+i}$, which only requires knowledge of the ratio of δ/β . This method will be referred to as C-NLPR/One- γ .

3) *C-NLPR / TrOpt- α, γ* : For this constraint, we control the dynamic range of \mathbf{z} depending on the known values for δ and β . We set α and β such that \mathbf{z}_n approximately varies between a preset low value of T_l and a high of 1. In this paper, we choose $T_l = 0.01$. Then, the values for α and γ are such that,

- $\mathbf{z}_n = 1$ in the absence of any material along the ray path for the n^{th} pixel measurement.
- $\mathbf{z}_n = T_l$ when a material with refractive index decrement δ and absorption index β lies along the entirety of the n^{th} ray.

Ideally, \mathbf{z}_n should only vary between T_l and 1 in the absence of measurement non-idealities and a perfect choice for δ/β . In practice, \mathbf{z}_n varies approximately within this chosen transmission range, which reduces the risk of numerical instabilities. Thus, our choice for α and γ are,

$$\alpha = -\frac{2\pi}{\lambda \log(T_l)} \beta \Delta \max(N_u, N_v), \quad (19)$$

$$\gamma = -\frac{2\pi}{\lambda \log(T_l)} \delta \Delta \max(N_u, N_v), \quad (20)$$

where Δ is the pixel width. The number of pixels in the X-ray images along the u -axis and v -axis are N_u and N_v respectively. However, this particular choice of α and γ requires knowledge of both δ and β . In contrast, the previous two choices that are described in sections IV-B1 and IV-B2 only require knowledge of the ratio δ/β . The constraint obtained using equations (19) and (20) will be referred to as C-NLPR/TrOpt- α, γ (TrOpt indicates optimized transmission).

In section VI, we demonstrate that $\alpha = 1, \gamma = \frac{\delta}{\beta}$ provides the best trade-off between stable optimization and good performance while only requiring knowledge of the ratio δ/β .

C. Optimization Algorithm

We implemented our NLPR algorithms using python programming language and *PyTorch* framework [37]. *PyTorch* uses algorithmic differentiation (or automatic differentiation) to compute gradients of the objective functions that are used for minimization. In equation (16), algorithmic differentiation is used to compute the gradient of $l(\mathbf{y}; \mathbf{x})$ with respect to \mathbf{x} .

Similarly, algorithmic differentiation is used to compute the gradient of $l(\mathbf{y}; \mathbf{z})$ with respect to \mathbf{z} in equation (18).

We use the LBFGS algorithm [38], [39] to solve the optimization problems in equations (16) and (18). The gradients computed using algorithmic differentiation are used by the LBFGS optimization algorithm to reconstruct \mathbf{x} in (16) and \mathbf{z} in (18). In this paper, we use the LBFGS implementation in [40] with a history size of 64. The maximum number of iterations is capped at 10^4 and we use Wolfe line search for optimal selection of step-size. We use a convergence criteria that automatically stops the LBFGS iterations based on the convergence of reconstruction and objective function values. We stop LBFGS when the following conditions are met for M consecutive iterations,

- Average of the absolute differences in the reconstruction (\mathbf{z} in C-NLPR or \mathbf{x} in U-NLPR), expressed as a percentage, is less than L_r . The difference is computed between the reconstructions at consecutive two iterations.
- The absolute difference in the objective function ($l(\mathbf{y}; \mathbf{z})$ in C-NLPR or $l(\mathbf{y}; \mathbf{x})$ in U-NLPR), expressed as a percentage, is less than L_c .

In this paper, we choose $M = 5$, $L_c = 1\%$, and $L_r = 0.5\%$ for all the simulated and experimental results in section VI. We recognize that this particular setting for the convergence criteria may appear overly stringent. Our particular choice was designed to ensure sufficient convergence for all data presented in this paper. However, for any given data set, the convergence criteria may be relaxed for reduced run-time.

D. Estimation of Phase and Absorption

To perform tomographic reconstruction, we need to estimate discrete sampled representations of $A(u, v)$ and $\phi(u, v)$ (from equation (2)). Let the vectors \mathbf{A} and ϕ be the discrete representations of $A(u, v)$ and $\phi(u, v)$ in raster order.

1) *U-NLPR*: The X-ray absorption, $\hat{\mathbf{A}}$, and phase shift, $\hat{\phi}$, that is induced by the object on the incident X-ray field is,

$$\hat{\mathbf{A}} = -\log(|\hat{\mathbf{x}}|) \text{ and } \hat{\phi} = -\tan^{-1}\left(\frac{\hat{\mathbf{x}}^{(I)}}{\hat{\mathbf{x}}^{(R)}}\right), \quad (21)$$

where $\hat{\mathbf{x}}^{(I)}$ and $\hat{\mathbf{x}}^{(R)}$ are the imaginary and real parts of $\hat{\mathbf{x}}$ respectively. Here, $\log(\cdot)$ and $\tan^{-1}(\cdot)$ ⁴ are element-wise vector operators. We use phase unwrapping [42], [43] to unwrap the phase images $\hat{\phi}$ prior to tomographic reconstruction.

2) *C-NLPR*: The X-ray absorption and phase images for C-NLPR are computed as,

$$\hat{\mathbf{A}} = -\alpha \log(\hat{\mathbf{z}}) \text{ and } \hat{\phi} = -\gamma \log(\hat{\mathbf{z}}). \quad (22)$$

Since the phase $\hat{\phi}$ obtained using equation (22) is already unwrapped, we do not need to apply an explicit phase unwrapping procedure.

Note that equations (21) and (22) are for a single angular view of the CT scan. Hence, we need to repeatedly apply equations (21) and (22) to compute the absorption and phase images for each view independently.

⁴We use `numpy.arctan2(·)` function of numpy [41]. It is the signed angle between the ray from the origin to (1, 0) and the ray from the origin to the point-of-interest.

V. TOMOGRAPHIC RECONSTRUCTION

In XPCT, measurement data is acquired at several rotation angles of the object. Let $\phi^{(n)}$ and $\mathbf{A}^{(n)}$ denote the phase and absorption images at view index n . From equations (21) and (22), $\hat{\phi}^{(n)}$ and $\hat{\mathbf{A}}^{(n)}$ are the estimated projections of the refractive index decrement and absorption index at view n . From equation (2), we see that the phase-shift and absorption are linear projections of the refractive index decrement and absorption index respectively. Filtered back projection (FBP) [13] is a popular algorithm that is widely used for reconstruction of X-ray absorption index from its linear projections. Thus, we use FBP to also reconstruct the refractive index decrement from its linear projections $\phi^{(n)}$ at all the views. In this paper, we do not investigate reconstruction of the absorption index due to poor absorption contrast.

A. Low-Frequency Information Loss

The reconstruction of refractive index decrement produced by U-NLPR and FBP may contain low-frequency artifacts. These artifacts have been well-documented in the research literature [12] on multi-distance phase-retrieval algorithms. Low-frequency artifacts refer to slowly varying spurious artifacts in the reconstructions due to the loss of low-frequency information in the measurements. Multi-distance phase-retrieval does not use material constraints such as the phase-absorption proportionality. Instead, they rely on measurements at a wide range of propagation distances for inversion.

We will investigate the loss of low-frequency information using the transfer function in equation (3). Equation (3) expresses the X-ray field $F_D(\mu, \nu)$ at the detector as a function of the X-ray field at the exit-plane of the object $F_O(\mu, \nu)$ in Fourier space. In the limit as the frequency components μ and ν approach zero, we have,

$$\mu \rightarrow 0 \text{ and } \nu \rightarrow 0 \implies F_D(\mu, \nu) \rightarrow F_O(\mu, \nu). \quad (23)$$

Thus, the value for $F_D(\mu, \nu)$, in the limit of zero frequencies, does not change with the propagation distance R since R is a parameter of only the Fresnel transfer function in equation (3). The detector only measures X-ray intensities, i.e., $|f_D(u, v)|^2$ (equation (4)). To compensate for this loss in phase information, we acquire measurements at varying propagation distances R such that the phase-contrast fringes vary in magnitude and thickness. The phase information that is encoded in the phase-contrast fringes can be retrieved by acquiring data at multiple distances. However, since $F_D(\mu, \nu)$ does not vary sufficiently with distance R at the low frequencies, we obtain low-frequency artifacts in the reconstruction due to insufficient information.

During phase-retrieval, we cannot reconstruct the average value of the phase irrespective of the number of multi-distance measurements. Let us represent the phase $\phi(u, v)$ as the sum of a constant ϕ_0 and a zero-mean phase term $\tilde{\phi}(u, v)$, i.e.,

$$\phi(u, v) = \phi_0 + \tilde{\phi}(u, v) \text{ s.t. } \int_{u,v} \tilde{\phi}(u, v) du dv = 0. \quad (24)$$

The constant phase term ϕ_0 factors out as the scalar multiple $\exp\{-i\phi_0\}$ in equations (1) and (3). Since the detector

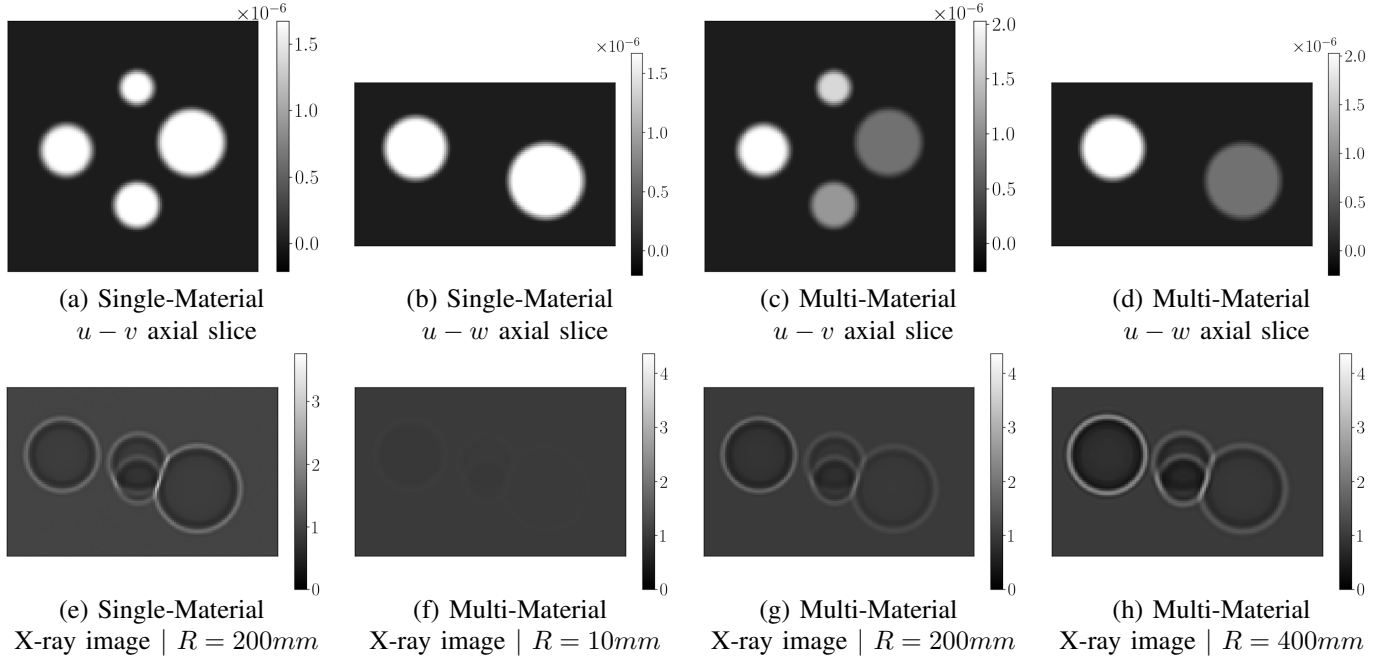


Fig. 2. Simulation of phase-contrast CT data. (a, b) and (c, d) show the simulated single-material homogeneous object and the multi-material heterogeneous object respectively. (a, c) show a planar slice ($u-v$ axes) perpendicular to the rotation axis and (b, d) show a planar slice ($u-w$ axes) parallel to the rotation axis. The slices in (a-d) pass through the center of the object. For the single-material object, the normalized X-ray image at a propagation distance, R , of $200mm$ is shown in (e). For the multi-material object, the normalized X-ray images at propagation distances of $10mm$, $200mm$, and $400mm$ are shown in (f), (g), and (h) respectively. All X-ray images in (e-h) are at the first tomographic view. Phase-contrast fringes are visible in (e), (g), and (h). From (f-h), we observe that increasing R also increases the strength of phase-contrast.

measurements $\tilde{y}(j, k)$ in equation (4) measure only the X-ray intensity, information on $\exp\{-i\phi_0\}$ is lost since $\exp\{-i\phi_0\}$ is a multiplying factor for $f_D(j\Delta, k\Delta)$.

B. Quantitative Evaluation

Our approach to extracting quantitative information from the refractive index decrement reconstructions is to compare the reconstructed values for the material-of-interest with the reconstructed values of the background air. We assume that the refractive index decrement of the background air is 0. Unfortunately, this process cannot be automated since determination of the background air region is non-trivial and application dependent. First, we compute the average value of the reconstruction in the background, denoted as $\delta^{(bg)}$. Next, we compute the average value of the reconstruction inside the material-of-interest, denoted as $\delta^{(m)}$. Finally, we compute the background corrected refractive index decrement of the material-of-interest as,

$$\delta^{(m:diff)} = \delta^{(m)} - \delta^{(bg)}. \quad (25)$$

Background subtraction is necessary due to the loss of the average value for the refractive index in the reconstruction. After background subtraction, $\delta^{(m:diff)}$ is the quantitatively accurate refractive index decrement that is comparable to the theoretical values.

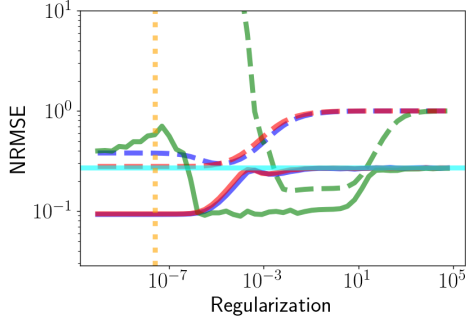
VI. RESULTS

A. Simulated Data

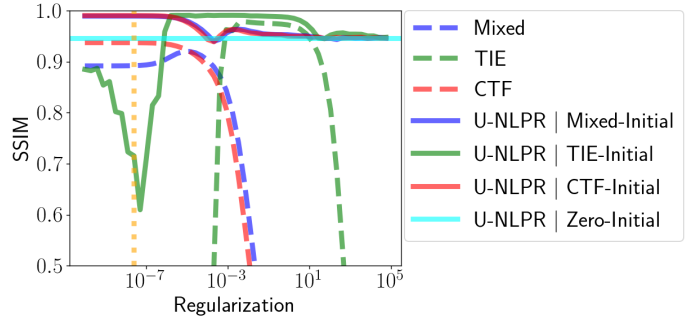
In this section, we compare the performance of our new NLPR algorithms against existing approaches using simulated

phase-contrast CT data of a 3D object at a monochromatic X-ray energy of $20keV$. To avoid using the same forward model for both simulation and inversion, we simulate X-ray images from more finely sampled objects of size $160 \times 256 \times 256$ and voxel size of $0.3225\mu m$ using equation (9). The simulated phase-contrast CT data, the stack of X-ray images over all views, is then sub-sampled to a size of $128 \times 80 \times 128$ by block-averaging the simulated images over non-overlapping square-shaped windows of pixels. Finally, we simulate Poisson-like noise in the measurements by adding zero-mean Gaussian noise with a standard deviation that is 0.1% of the simulated data (equation (10)).

Cross-sectional slices through the simulated object along with the corresponding simulated X-ray images with phase-contrast are shown in Fig. 2. First, we simulate a single-material object (Fig. 2 (a, b)) that consists of several spheres with differing diameters but made using the same material. The material used for the spheres is SiC with a refractive index decrement (δ) of 1.67×10^{-6} and absorption index (β) of 4.77×10^{-9} at an X-ray energy of $20keV$. For this object, the normalized X-ray image with phase-contrast at a propagation distance of $R = 200mm$ is shown in Fig. 2 (e). Next, we simulate a multi-material object (Fig. 2 (c, d)) that consists of four spheres with varying diameters and differing atomic composition. For the spheres, we chose SiC ($\delta = 1.67 \times 10^{-6}$, $\beta = 4.77 \times 10^{-9}$), Teflon ($\delta = 1.1 \times 10^{-6}$, $\beta = 9.09 \times 10^{-10}$), Alumina ($\delta = 2.03 \times 10^{-6}$, $\beta = 3.97 \times 10^{-9}$), and Polyimide ($\delta = 7.61 \times 10^{-7}$, $\beta = 3.21 \times 10^{-10}$) as the materials. The X-ray images with phase-contrast for this heterogeneous object are shown in Fig. 2 (f-h) at propagation distances, R , of



(a) NRMSE vs. Regularization of Conventional PR



(b) SSIM vs. Regularization of Conventional PR

Fig. 3. Quantitative comparison of the refractive index decrement reconstructions using various phase-retrieval (PR) algorithms. (a) and (b) shows the normalized root mean squared error (NRMSE) and structural similarity index measure (SSIM) as a function of the regularization parameter, α' , for the various PR methods. Lower is better for NRMSE and higher is better for SSIM. Both NRMSE and SSIM are computed for the entire volume of the foreground spheres after background subtraction (section V-B). The dashed lines show the NRMSE and SSIM for the conventional methods [12] of Transport of Intensity Equation (TIE), Contrast Transfer Function (CTF), and Mixed phase-retrieval. The solid lines show the NRMSE and SSIM for U-NLPR that is initialized using either TIE, CTF, Mixed, or zero phase/absorption values (indicated in the legend of (b)). Since U-NLPR does not use any regularization, the regularization parameter along the horizontal axis of (a, b) belongs to the conventional PR methods used for initialization. The vertical dotted orange line indicates the fixed choice for the regularization α' as defined in equation (17). U-NLPR consistently out-performs the conventional PR method used for initialization.

Multi-distance Phase-Retrieval (PR) followed by FBP Reconstruction of the Multi-Material Object

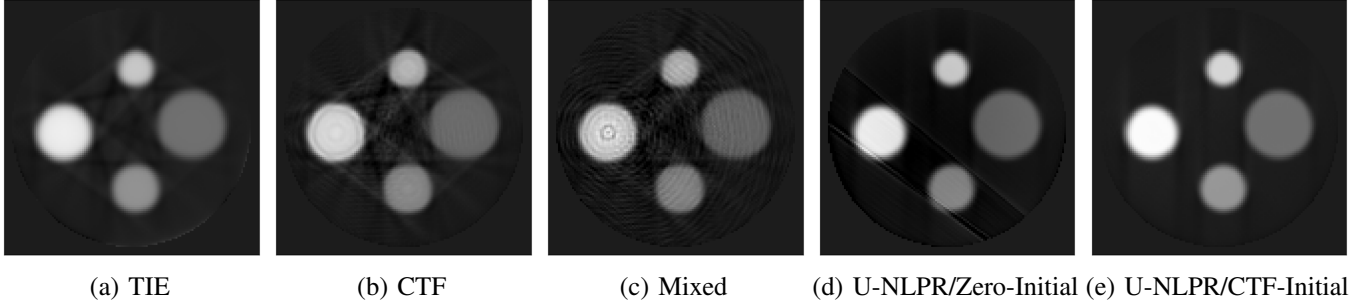


Fig. 4. Tomographic reconstructions of the refractive index decrement from the phase images produced by the CTF, TIE, Mixed, and U-NLPR (proposed) phase-retrieval (PR) algorithms. (a-e) show planar slices along the $u-v$ axes that pass through the center of the reconstruction volume. (a), (b), and (c) are using the TIE, CTF, and Mixed PR algorithms respectively. For the conventional PR methods of TIE, CTF, and Mixed, we present the best performing reconstruction with the highest SSIM (from Fig. 3). (d) shows the reconstruction using U-NLPR that is initialized with zeros for the phase and absorption. (e) shows the reconstruction using U-NLPR that is initialized with CTF at the fixed regularization in equation (17). The gray values in (a-e) are scaled between -2.53×10^{-7} and 2.03×10^{-6} . Compared to the conventional PR reconstructions in (a-c), U-NLPR reduces streak artifacts and noise as shown in (d, e). Reconstruction slices along the $u-w$ axes are shown in Fig S1 of the supplementary document.

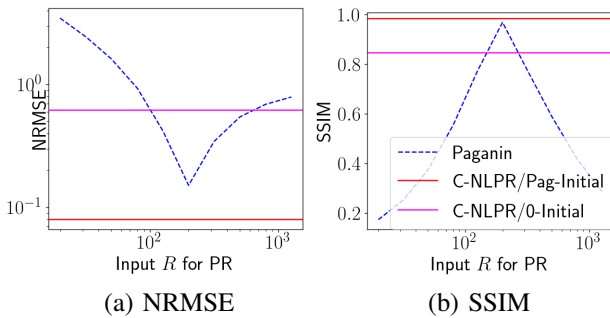


Fig. 5. NRMSE and SSIM between reconstruction and ground-truth for the refractive index decrement as a function of the (inaccurate) propagation distance R that is input to the phase retrieval (PR) algorithms. The true propagation distance R used for simulation is 200mm . The NRMSE is lowest and SSIM is highest when R is set equal to its true value of 200mm . Initializing C-NLPR with zeros for the phase results in sub-optimal performance that is worse than Paganin PR. C-NLPR initialized with Paganin PR has the best performance.

10mm , 200mm , and 400mm . For both the single and multi-material objects, the radii of the spheres were chosen to be $12\mu\text{m}$, $16\mu\text{m}$, $20\mu\text{m}$, and $24\mu\text{m}$ respectively. We simulate X-ray images of size 80×128 with pixel width of $1.29\mu\text{m}$ at 128 tomographic views equally spaced over an angular range of 180° . For phase-retrieval (PR), we use the square root of the normalized X-ray images computed using equation (5).

A quantitative comparison of the refractive index decrement reconstructions using various multi-distance phase-retrieval algorithms is presented in Fig. 3. At each tomographic view, we use phase-retrieval to estimate the phase images that are a measure of the phase-shift induced by the object on the X-ray field. Then, we use filtered back projection (FBP) to perform a tomographic reconstruction of the refractive index decrement from the phase images. Fig. 3 (a) is the normalized root mean squared error (NRMSE)⁵ between the reconstructions and the ground-truth. Fig. 3 (b) is the structural

⁵NRMSE is normalized using the averaged l^2 norm of the ground-truth.

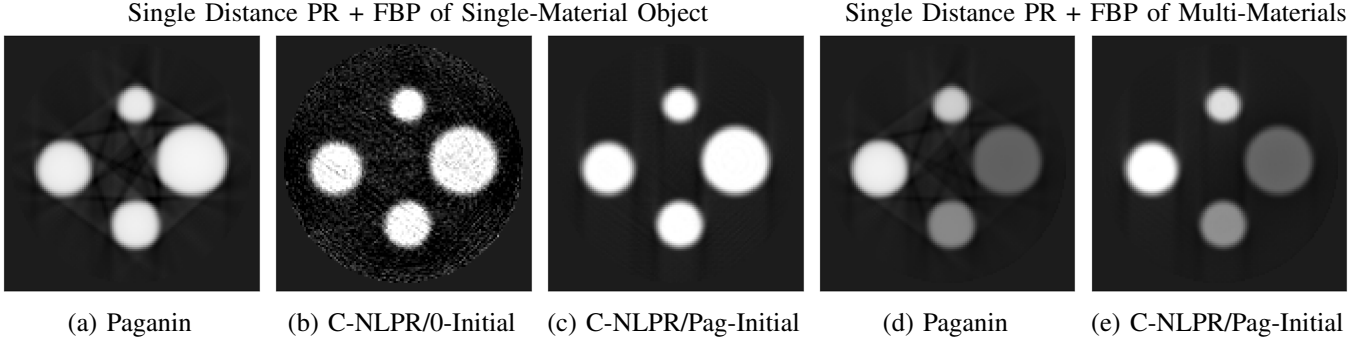


Fig. 6. Tomographic reconstructions of the refractive index decrement from the phase images produced by the single-distance phase-retrieval (PR) algorithms of Paganin and C-NLPR (proposed). (a-c) show reconstructions of the single material object. (d, e) show reconstructions of the multi-material object. (a-e) show planar slices along the $u-v$ axes that pass through the center of the reconstruction volume. (a) and (d) show reconstructions using Paganin PR. (b) shows the reconstruction using C-NLPR that is initialized with zeros for the phase image (label C-NLPR/0-Initial). (c) and (e) show reconstructions using C-NLPR with Paganin initialization produces the best reconstruction that minimize noise and artifacts.

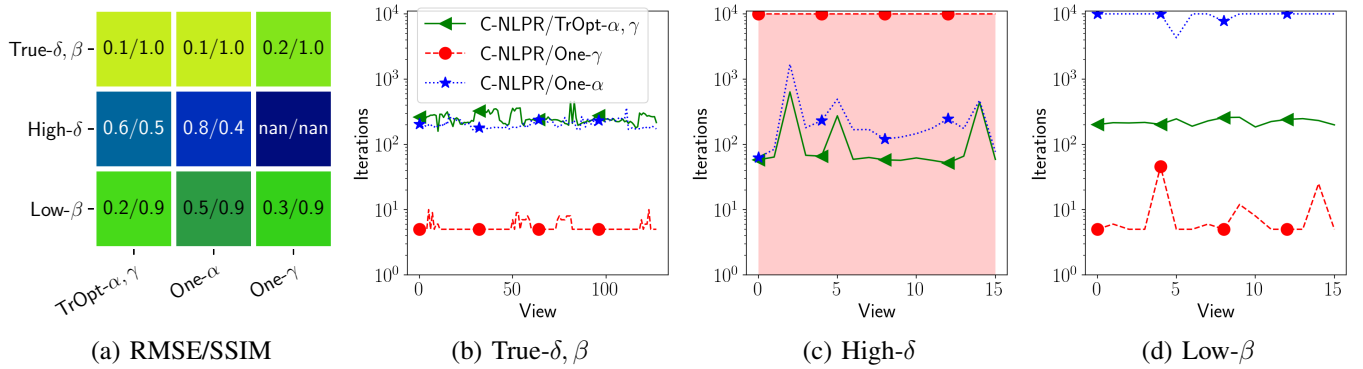


Fig. 7. Quantification of performance and convergence speed of C-NLPR for various choices of α and γ as described in sections IV-B1, IV-B2, and IV-B3. Our analysis is repeated for various δ, β values. True- δ, β uses the ground-truth δ, β of SiC. High- δ refers to a δ that is $10\times$ the δ of SiC. Low- β refers to a β that is $0.02\times$ the β of SiC. (a) shows the RMSE (left of /) and SSIM (right of /) performance metrics. (b, c, d) show the number of LBFGS iterations as a function of the view index. Corrupted reconstructions caused by numerical instabilities is indicated by “nan” (not-a-number) in (a) and shaded with a translucent color in (c). From (a, c), we see that C-NLPR/One- γ results in “nan” due to numerical instabilities for High- δ . With C-NLPR/One- α , while we achieve good overall performance in (a), the number of iterations may reach large numbers for Low- β as shown in (d). For C-NLPR/TrOpt- α, γ , we achieve good overall performance in (a) with reduced number of iterations in (b, c, d). Legend for (c, d) is same as in (b).

similarity index measure (SSIM)⁶. We use the NRMSE and SSIM implementations from *scikit-image* [43]. We compute NRMSE and SSIM for the entire volume of the spheres after background subtraction as described in the section V-B. We exclude regions close to the edges of the spheres when computing the refractive index decrements in equation (25). For the conventional phase-retrieval methods [12] of CTF, TIE, and Mixed, we plot (dashed lines) the NRMSE and SSIM measures as a function of its regularization parameter. To adequately reduce NRMSE and increase SSIM using TIE phase retrieval, we must carefully tune its regularization hyper-parameter to lie within a narrow range of parameter values. An arbitrary choice of either a very low or high parameter value for regularization will lead to sub-optimal results with TIE. For CTF and Mixed phase retrieval, it is possible to achieve low NRMSE and high SSIM by choosing a sufficiently small value for the regularization. As the regularization parameter is reduced, the performance of CTF does not degrade while Mixed leads to

marginal reduction in performance. For CTF, we can minimize the NRMSE and maximize SSIM by choosing a sufficiently small fixed value for the regularization parameter. In particular, we fix the regularization parameter value using (17) to avoid the need for parameter tuning.

We use U-NLPR from section IV-A for multi-distance phase-retrieval without any material constraints. The performance of U-NLPR is influenced by the estimates of the phase and absorption that is used for initialization of the optimization in equation (16). In Fig. 3, we investigate the use of phase images from CTF, TIE, or Mixed phase-retrieval as initial estimates for initialization of U-NLPR. The performance of these conventional methods is dependent on the chosen value of the regularization parameter. In Fig. 3, we plot (solid lines) the NRMSE and SSIM for U-NLPR as a function of the regularization parameter of the conventional method (i.e., CTF, TIE, and Mixed) used for initialization. We observe that U-NLPR always produces lower NRMSE and higher SSIM when compared to the estimates from the method used for initialization. Importantly, we observe that the best performance of U-NLPR is achieved by initialization using the CTF algorithm

⁶For SSIM, the inputs are linearly scaled such that the minimum and maximum values of ground-truth are mapped to -1 and 1 respectively. We use Gaussian weights with standard deviation of 8 pixels.

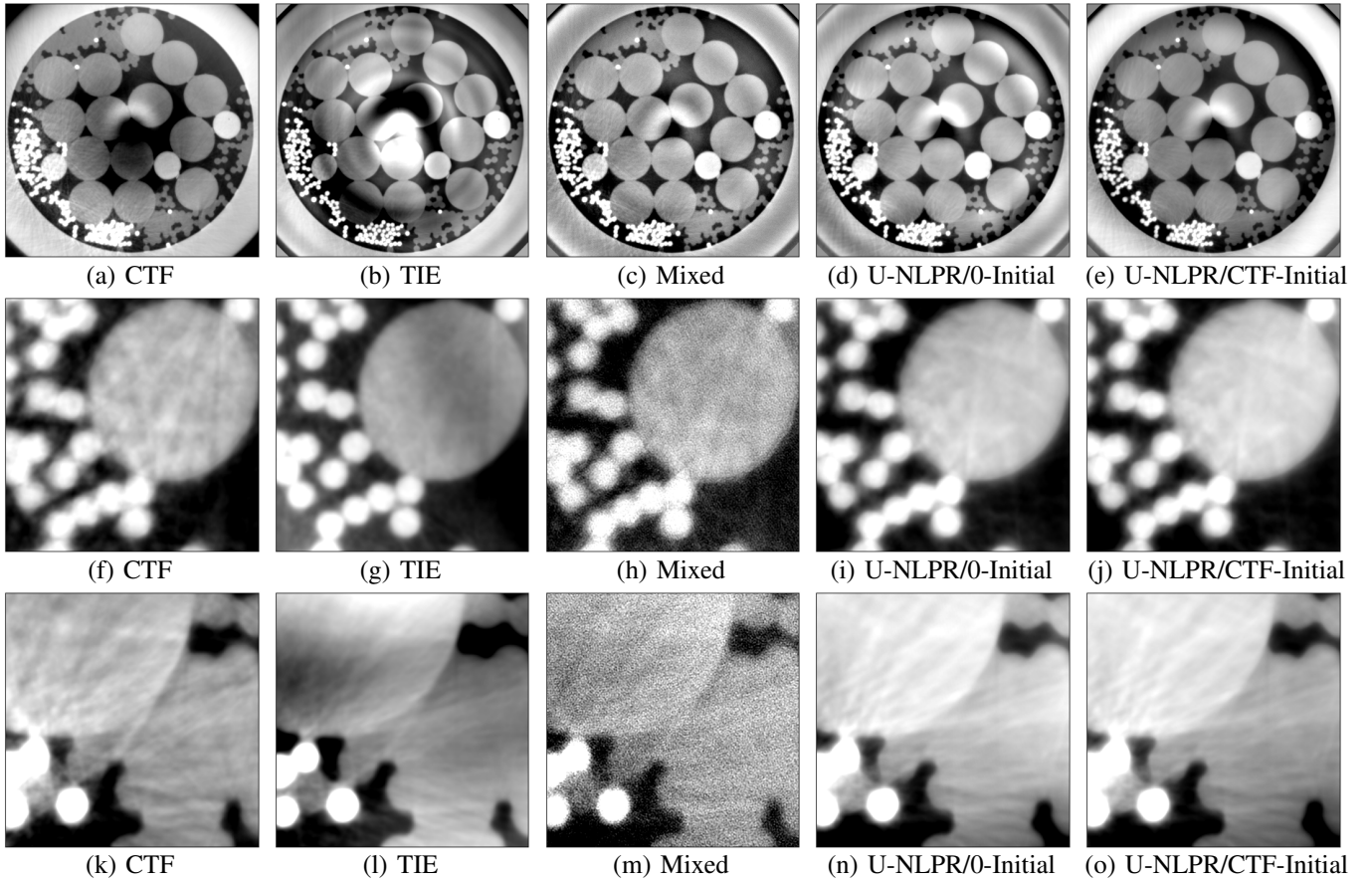


Fig. 8. Experimental data reconstruction comparison of the refractive index decrement for various multi-distance phase-retrieval (PR) algorithms. (a-e) show planar reconstruction slices along the $u - v$ axes passing through the center of the volume. The reconstruction in (a-e) is cropped to show the region within the interior of the sample holder. (f-j) and (k-o) zooms into two different regions of the reconstructions in (a-e). Since the quantitative values vary substantially between PR methods (see section V-A), we scale the gray values of each image individually between the value percentiles of 5% and 95%. Both CTF and TIE produce substantial low-frequency artifacts in (a), (b), (g), and (l). Mixed reduces the artifacts but has increased noise as shown in (h, m). U-NLPR, irrespective of the initialization, produces the best reconstructions that minimize noise and artifacts. In particular, U-NLPR with CTF initialization (using the fixed regularization in equation (17)) produce less intense artifacts at the center of the images in (d, e) when compared to zero-initialization.

with a sufficiently low value for the regularization as specified in equation (17). While the Mixed approach may also be suitable for initialization, we prefer the CTF approach due to the ease of choosing the regularization using equation (17). Note that the SSIM with Mixed PR decreases slightly at very low regularization values.

The reconstructions with the highest SSIM using the conventional phase retrieval algorithms of TIE, CTF, and Mixed approaches are shown in Fig. 4 (a-c). In Fig. 4 (d), we show the reconstruction using U-NLPR that is initialized with zero values for the phase and absorption. In Fig. 4 (e), we show the U-NLPR reconstruction that is initialized using CTF phase-retrieval that used the regularization of equation (17). Since U-NLPR does not use any regularization, we avoid the need for the tedious manual tuning of regularization hyperparameters. From Fig. 4 (a-c) and Fig. 2 (c), we observe that conventional phase-retrieval methods produce spurious streak artifacts. While the artifacts are faint in the case of TIE, both CTF and Mixed produce strong streak artifacts. When initialized with zeros for the phase and absorption, U-NLPR in Fig. 4 (d) produce a better reconstruction with significantly fewer streak artifacts than the conventional methods. When

initialized using CTF with the fixed regularization of equation (17), U-NLPR produces the best reconstruction with reduced artifacts as shown in Fig. 4 (e).

We visually compare the tomographic reconstruction performance of single-distance phase retrieval algorithms in Fig. 6. Qualitative comparisons of phase-retrieval methods for single-material object and multi-material objects are shown in Fig. 6 (a-c) and Fig. 6 (d, e) respectively. Paganin phase-retrieval produces streak artifacts as shown in Fig. 6 (a, d). We investigate the performance of C-NLPR from section IV-B for non-linear phase-retrieval using the single-material constraint. If C-NLPR is initialized with zeros for the phase images, C-NLPR reduces artifacts but significantly enhances the noise in Fig. 6 (b). C-NLPR using Paganin phase-retrieval for initialization provides the best quality reconstruction as shown in Fig. 6 (c, e). We use the C-NLPR/One- α method from section IV-B1 in Fig. 6. Surprisingly, we also observe that the qualitative performance does not degrade for multi-material object.

Fig. 5 performs a quantitative analysis of the reconstruction performance for various single-distance phase-retrieval algorithms. With Paganin phase-retrieval, it is common to achieve

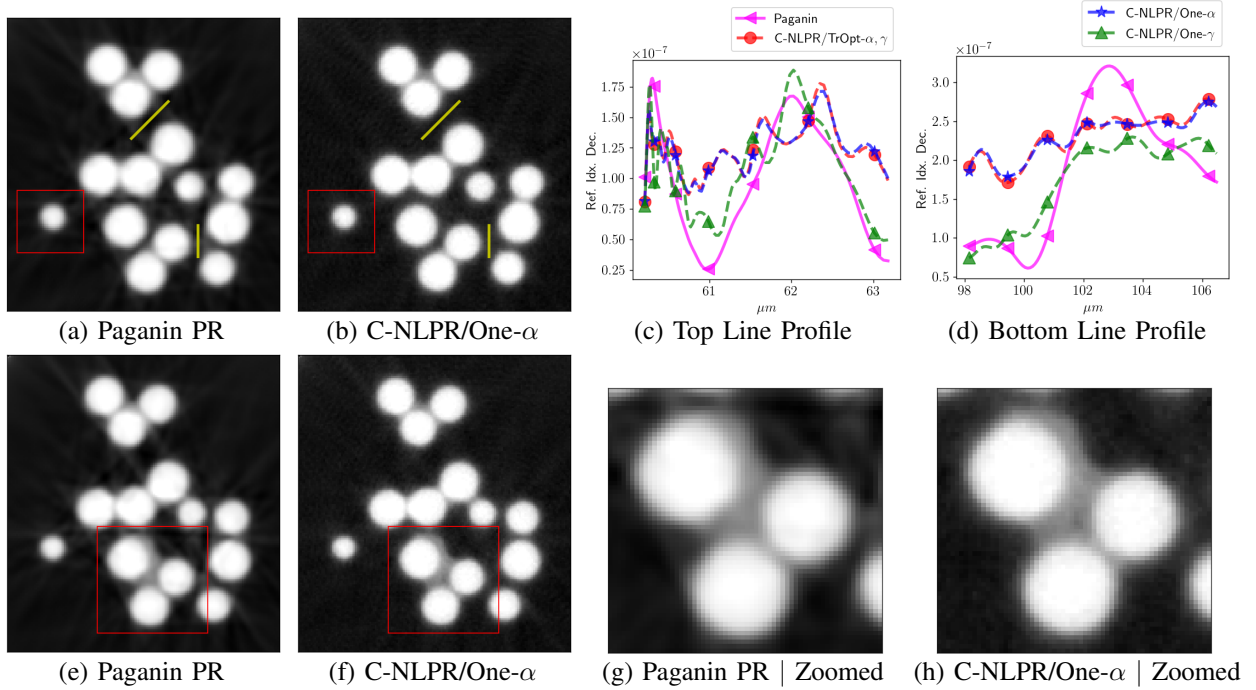


Fig. 9. Tomographic reconstruction of the refractive index decrement from phase images retrieved using single-distance phase-retrieval (PR) methods. (a) and (b) show the center slice ($u-v$ axes) of the reconstruction using Paganin PR and C-NLPR/One- α respectively. (c) and (d) show line profile comparisons between Paganin and C-NLPR along the yellow marked lines in (a) and (b). In (c, d), the large dynamic range for Paganin and C-NLPR/One- γ indicate the presence of streak artifacts since these line-profiles are in the background region of (a, b). Both C-NLPR/TrOpt- α, γ and C-NLPR/One- α reduces streaking artifacts as illustrated in (c, d). (e) and (f) show the reconstructions along a different slice in the presence of a second material between the SiC fibers. (g, h) zooms into the region within the red squares in (e, f) and demonstrates the sharper reconstruction using C-NLPR/One- α when compared to Paganin PR. Images in (a, b, e-h) are scaled between -1.79×10^{-7} and 1.43×10^{-6} . (c, d) use a common legend that is indicated at the top of the plots.

sharper reconstructions by artificially lowering the propagation distance, R , that is input to the algorithm. However, from Fig. 5, we see that an inaccurate setting for R compared to its true value leads to sub-optimal NRMSE and SSIM values. The best performance for Paganin is achieved when R is set equal to the true propagation distance of 200mm . Initializing C-NLPR with Paganin phase-retrieved images results in the lowest NRMSE and highest SSIM among all approaches. However, initializing C-NLPR with zero phase images produces sub-optimal reconstructions with large amounts of noise as shown in Fig. 6 (b, g). In Fig. 5, we used the C-NLPR/One- α method described in section IV-B1.

The convergence speed and reconstruction quality of C-NLPR are strongly influenced by the choice of α and γ as evidenced in Fig. 7. Fig. 7 (a) compares the NRMSE and SSIM for different constraint choices of C-NLPR/TrOpt- α, γ (section IV-B3), C-NLPR/One- α (section IV-B1), and C-NLPR/One- γ (section IV-B2). The rows of Fig. 7 (a) correspond to different choices for the material properties of δ, β while the columns cycle through the various α, γ settings used for imposing the single-material constraint. The row label “True- δ, β ” indicates that the simulated object used the true δ, β values for SiC at 20keV . The label “High- δ ” indicates a very large value for δ that is $10\times$ higher than the δ of SiC. The label “Low- β ” indicates a very low value for β that is $1/50\times$ the β of SiC. For the various materials characterized by its δ, β values, we see that C-NLPR/TrOpt- α, γ consistently produces the lowest NRMSE. Using the SSIM measure, the results

are a tie between C-NLPR/TrOpt- α, γ and C-NLPR/One- α . However, the latter only uses knowledge of the ratio δ/β .

In Fig. 7 (b-d), we plot the number of iterations for the LBFGS optimization algorithm as a function of the tomographic view index. Fig. 7 (b), Fig. 7 (c), and Fig. 7 (d) are the convergence plots for “True- δ, β ”, “High- δ ”, and “Low- β ” respectively. For the true values of δ, β of SiC, C-NLPR/One- γ has the fastest convergence in Fig. 7 (b) but increased NRMSE in the first row of Fig. 7 (a). In contrast, both C-NLPR/TrOpt- α, γ and C-NLPR/One- α converge slower but achieve lower NRMSE. From Fig. 7 (c) and second row of Fig. 7 (a), we see that numerical instabilities associated with C-NLPR/One- γ result in slow convergence and corrupted reconstructions due to the high δ value (see section IV-B2). From Fig. 7 (c), C-NLPR/One- α is slow to converge, but has a high SSIM as indicated in the third row of Fig. 7 (a) (see section IV-B1). The maximum number of iterations was fixed at 10^4 for the LBFGS optimization. While C-NLPR/TrOpt- α, γ has the best convergence for all cases, it requires knowledge of both δ and β . Alternatively, C-NLPR/One- α only uses knowledge of the ratio δ/β while also matching C-NLPR/TrOpt- α, γ in convergence speed for “True- δ, β ” and “High- δ ”.

B. Experimental Data

For comparison of phase-retrieval methods using experimental data, a bundle of fibers comprising PolyEthylene Terephthalate (PET), polypropylene (PP), Aluminum (Al), and Aluminum Oxide (Al_2O_3) with respective diameters of

200 μm , 28 μm , 125 μm , and 20 μm were enclosed in a borosilicate capillary glass and scanned for tomography at the X-ray imaging beamline 8.3.2 of the Advanced Light Source, Berkeley, California. Monochromator was set to deliver X-ray beam with energy of 22keV. A PCO edge camera combined with 10 \times lens was used to collect X-ray images, resulting in an effective pixel size of approximately 0.65 μm . A total number of 1312 X-ray images were recorded over 180 $^\circ$ range and using a 500ms exposure time. Object was placed at approximately 21m from the X-ray source and detector was moved at object-to-detector propagation distances of 30mm, 100mm, and 250mm for each scan. The size of each X-ray image was 1686 \times 2532. The normalized X-ray images are shown in Fig. S3 of the supplementary document.

Tomographic reconstructions of the refractive index decrement from phase images reconstructed using various multi-distance phase-retrieval algorithms are shown in Fig. 8. The regularization parameters for the conventional phase-retrieval methods of CTF, TIE, and Mixed are manually tuned to obtain the best visual quality of reconstructions. Substantial low-frequency reconstruction artifacts are observed in Fig. 8 (a, b, g, l) for CTF and TIE phase-retrieval. Mixed phase-retrieval produces large amounts of reconstruction noise as shown in the zoomed images of Fig. 8 (h, m). We note that the noise with Mixed can be reduced by adjusting the regularization but it also severely reduces the quality of reconstruction. U-NLPR produces the best reconstructions in Fig. 8 (d, e, i, j, n, o) that substantially reduces both low-frequency artifacts and noise when compared to the conventional methods. Surprisingly, U-NLPR with zero-initialization results in a similar level of reconstruction quality as U-NLPR that is initialized using CTF with regularization from equation (17). Note that some of the artifacts in the centers of Fig. 8 (a-e) are ring artifacts [44] and we do not explore the correction of ring artifacts in this paper. The complicated interaction between ring-artifact removal and phase-retrieval algorithms necessitate further investigation. Fig. S4 in the supplementary document presents a quantitative comparison of the phase-retrieval performance.

For comparison of single-distance phase-retrieval algorithms, we obtained experimental X-ray CT data with phase-contrast from the Advanced Light Source (ALS) Beamline 8.3.2. CT data of SiC fibers was acquired at an object-to-detector distance of $R = 98\text{mm}$ and X-ray energy of 20keV. The size of each X-ray image was 324 \times 320 and the pixel width was 0.645 μm . X-ray images were acquired at 256 different views equally spaced over an angular range of 180 degrees. A normalized X-ray image is shown in Fig. S5. of the supplementary document.

Tomographic reconstructions of the refractive index decrement from phase images reconstructed using various single-distance phase-retrieval algorithms are shown in Fig. 9. Fig. 9 (a, e) and (b, f) show the reconstructions using Paganin and C-NLPR/One- α respectively. The line profiles in Fig. 9 (c, d) are along the yellow lines in Fig. 9 (a, b). They highlight the reduction in streak artifacts using C-NLPR/One- α when compared to Paganin phase-retrieval. The zoomed images in Fig. 9 (g, h) also demonstrate the significant enhancement in sharpness using C-NLPR/One- α even in the presence of

a second material that is not modeled by the constraints of C-NLPR. Fig. S6 in the supplementary document presents a quantitative analysis of the reconstruction sharpness and the speed of algorithm convergence.

VII. CONCLUSION

For propagation-based X-ray phase-contrast tomography (XPCT), we presented new non-linear phase-retrieval algorithms (NLPR) to reconstruct the phase-shift induced by the object on the X-ray field. Then, we demonstrated reconstruction of the refractive index decrement in 3D from the phase-shift images using tomographic reconstruction algorithms. Our approaches do not require any manual tuning of image quality related hyper-parameters such as regularization. Our NLPR algorithms are suitable for both single-distance and multi-distance XPCT while also supporting explicit constraints on the material composition. For single-distance XPCT, we demonstrated phase-retrieval (PR) under the constraint of single-material or phase-absorption proportionality. Our NLPR algorithms produced the best reconstructions based on both quantitative metrics of accuracy as well as qualitative evaluation of artifact reduction. The superior performance of NLPR is a result of employing non-linear measurement models that are more accurate than the linear approximations made by existing linear PR approaches. For multi-distance XPCT, we show that zero-initialization of the phase for NLPR may be sufficient, but the best performance is achieved by initializing with the Contrast Transfer Function (CTF) PR. For single-distance XPCT, we show that NLPR produces the best reconstruction when initialized with Paganin PR.

ACKNOWLEDGMENTS

LLNL-JRNL-847272. This work was performed under the auspices of the U.S. Department of Energy by Lawrence Livermore National Laboratory under Contract DE-AC52-07NA27344. This research used resources of the Advanced Light Source, which is a DOE Office of Science User Facility under contract no. DE-AC02-05CH11231.

REFERENCES

- [1] C. Karunakaran, R. Lahlali, N. Zhu, A. M. Webb, M. Schmidt, K. Fransishyn, G. Belev, T. Wysokinski, J. Olson, D. M. L. Cooper, and E. Hallin, "Factors influencing real time internal structural visualization and dynamic process monitoring in plants using synchrotron-based phase contrast X-ray imaging," *Scientific Reports*, vol. 5, no. 1, Jul. 2015.
- [2] L. C. P. Croton, K. S. Morgan, D. M. Paganin, L. T. Kerr, M. J. Wallace, K. J. Crossley, S. L. Miller, N. Yagi, K. Uesugi, S. B. Hooper, and M. J. Kitchen, "In situ phase contrast X-ray brain CT," *Scientific Reports*, vol. 8, no. 1, Jul. 2018.
- [3] L. Zielke, C. Barchasz, S. Waluś, F. Alloin, J.-C. Leprêtre, A. Spettl, V. Schmidt, A. Hilger, I. Manke, J. Banhart, R. Zengerle, and S. Thiele, "Degradation of Li/S Battery Electrodes On 3D Current Collectors Studied Using X-ray Phase Contrast Tomography," *Scientific Reports*, vol. 5, no. 1, p. 10921, Jun. 2015.
- [4] N. D. Parab, Z. A. Roberts, M. H. Harr, J. O. Mares, A. D. Casey, I. E. Gunduz, M. Hudspeth, B. Claus, T. Sun, K. Fezzaa, S. F. Son, and W. W. Chen, "High speed X-ray phase contrast imaging of energetic composites under dynamic compression," *Applied Physics Letters*, vol. 109, no. 13, p. 131903, Sep. 2016.

- [5] F. Sun, L. Zielke, H. Markötter, A. Hilger, D. Zhou, R. Moroni, R. Zengerle, S. Thiele, J. Banhart, and I. Manke, "Morphological Evolution of Electrochemically Plated/Stripped Lithium Microstructures Investigated by Synchrotron X-ray Phase Contrast Tomography," *ACS Nano*, vol. 10, no. 8, pp. 7990–7997, Aug. 2016.
- [6] D. S. Eastwood, P. M. Bayley, H. Jung Chang, O. O. Taiwo, J. Vila-Comamala, D. J. L. Brett, C. Rau, P. J. Withers, P. R. Shearing, C. P. Grey, and P. D. Lee, "Three-dimensional characterization of electrodeposited lithium microstructures using synchrotron X-ray phase contrast imaging," *Chemical Communications*, vol. 51, no. 2, pp. 266–268, 2015.
- [7] S. Pacilè, P. Baran, C. Dullin, M. Dimmock, D. Lockie, J. Missbach-Guntner, H. Quiney, M. McCormack, S. Mayo, D. Thompson, Y. Nesterets, C. Hall, K. Pavlov, Z. Prodanovic, M. Tonutti, A. Accardo, J. Fox, S. Tavakoli Tab, S. Lewis, P. Brennan, D. Hausermann, G. Tromba, and T. Gureyev, "Advantages of breast cancer visualization and characterization using synchrotron radiation phase-contrast tomography," *Journal of Synchrotron Radiation*, vol. 25, no. 5, pp. 1460–1466, Sep. 2018.
- [8] A. Bravin, P. Coan, and P. Suortti, "X-ray phase-contrast imaging: from pre-clinical applications towards clinics," *Physics in Medicine and Biology*, vol. 58, no. 1, pp. R1–R35, Dec. 2012.
- [9] V. Fernandez, E. Buffetaut, E. Maire, J. Adrien, V. Suteethorn, and P. Tafforeau, "Phase Contrast Synchrotron Microtomography: Improving Noninvasive Investigations of Fossil Embryos In Ovo," *Microscopy and Microanalysis*, vol. 18, no. 1, pp. 179–185, Feb. 2012.
- [10] E. M. Friis, P. R. Crane, K. R. Pedersen, S. Bengtson, P. C. J. Donoghue, G. W. Grimm, and M. Stamparoni, "Phase-contrast X-ray microtomography links Cretaceous seeds with Gnetales and Bennettitales," *Nature*, vol. 450, no. 7169, Nov. 2007.
- [11] A. Burvall, U. Lundström, P. A. C. Takman, D. H. Larsson, and H. M. Hertz, "Phase retrieval in X-ray phase-contrast imaging suitable for tomography," *Optics Express*, vol. 19, no. 11, pp. 10359–10376, May 2011.
- [12] M. Langer, P. Cloetens, J.-P. Guigay, and F. Peyrin, "Quantitative comparison of direct phase retrieval algorithms in in-line phase tomography," *Medical Physics*, vol. 35, no. 10, pp. 4556–4566, 2008.
- [13] A. C. Kak and M. Slaney, *Principles of Computerized Tomographic Imaging*. Society of Industrial and Applied Mathematics, 2001.
- [14] D. Paganin, S. C. Mayo, T. E. Gureyev, P. R. Miller, and S. W. Wilkins, "Simultaneous phase and amplitude extraction from a single defocused image of a homogeneous object," *Journal of Microscopy*, vol. 206, no. 1, 2002.
- [15] M. A. Beltran, D. M. Paganin, K. Uesugi, and M. J. Kitchen, "2D and 3D X-ray phase retrieval of multi-material objects using a single defocus distance," *Optics Express*, vol. 18, no. 7, pp. 6423–6436, Mar. 2010.
- [16] T. E. Gureyev, T. J. Davis, A. Pogany, S. C. Mayo, and S. W. Wilkins, "Optical phase retrieval by use of first Born- and Rytov-type approximations," *Applied Optics*, vol. 43, no. 12, p. 2418, Apr. 2004.
- [17] A. V. Bronnikov, "Reconstruction formulas in phase-contrast tomography," *Optics Communications*, vol. 171, no. 4, pp. 239–244, Dec. 1999.
- [18] X. Wu, H. Liu, and A. Yan, "X-ray phase-attenuation duality and phase retrieval," *Opt. Lett.*, vol. 30, no. 4, pp. 379–381, Feb. 2005.
- [19] P. Cloetens, P. Ludwig, E. Boller, L. Helfen, L. Salvo, R. Mache, and M. Schlenker, "Quantitative phase contrast tomography using coherent synchrotron radiation," in *Developments in X-Ray Tomography III*, vol. 4503. SPIE, Jan. 2002, pp. 82–91.
- [20] J. P. Guigay, M. Langer, R. Boistel, and P. Cloetens, "Mixed transfer function and transport of intensity approach for phase retrieval in the Fresnel region," *Optics Letters*, vol. 32, no. 12, p. 1617, Jun. 2007.
- [21] B. Yu, L. Weber, A. Pacureanu, M. Langer, C. Olivier, P. Cloetens, and F. Peyrin, "Evaluation of phase retrieval approaches in magnified X-ray phase nano computerized tomography applied to bone tissue," *Optics Express*, vol. 26, no. 9, pp. 11110–11124, Apr. 2018.
- [22] S. Zabner, P. Cloetens, J.-P. Guigay, J. Baruchel, and M. Schlenker, "Optimization of phase contrast imaging using hard x rays," *Review of Scientific Instruments*, vol. 76, no. 7, p. 073705, Jul. 2005.
- [23] M. Langer, P. Cloetens, and F. Peyrin, "Regularization of Phase Retrieval With Phase-Attenuation Duality Prior for 3-D Holotomography," *IEEE Transactions on Image Processing*, vol. 19, no. 9, pp. 2428–2436, Sep. 2010.
- [24] K. A. Mohan, X. Xiao, and C. A. Bouman, "Direct model-based tomographic reconstruction of the complex refractive index," in *2016 IEEE International Conference on Image Processing (ICIP)*, Sep. 2016, pp. 1754–1758.
- [25] V. Davidoiu, B. Sixou, M. Langer, and F. Peyrin, "Non-linear iterative phase retrieval based on Frechet derivative," *Optics Express*, vol. 19, no. 23, p. 22809, Nov. 2011.
- [26] —, "Non-linear iterative phase retrieval based on Frechet derivative and projection operators," in *2012 9th IEEE International Symposium on Biomedical Imaging (ISBI)*, May 2012, pp. 106–109.
- [27] —, "Nonlinear Phase Retrieval Using Projection Operator and Iterative Wavelet Thresholding," *IEEE Signal Processing Letters*, vol. 19, no. 9, pp. 579–582, Sep. 2012.
- [28] —, "Nonlinear approaches for the single-distance phase retrieval problem involving regularizations with sparsity constraints," *Applied Optics*, vol. 52, no. 17, p. 3977, Jun. 2013.
- [29] K. Mom, M. Langer, and B. Sixou, "Deep gauss-newton for phase retrieval," *Opt. Lett.*, vol. 48, no. 5, pp. 1136–1139, Mar. 2023.
- [30] Y. Wu, L. Zhang, S. Guo, L. Zhang, F. Gao, M. Jia, and Z. Zhou, "Enhanced phase retrieval via deep concatenation networks for in-line x-ray phase contrast imaging," *Physica Medica*, vol. 95, pp. 41–49, 2022.
- [31] R. Deshpande, A. Avachat, F. J. Brooks, and M. A. Anastasio, "Investigating the robustness of a deep learning-based method for quantitative phase retrieval from propagation-based x-ray phase contrast measurements under laboratory conditions," *Physics in Medicine & Biology*, 2023.
- [32] F. Li, Y. Zhao, S. Han, D. Ji, Y. Li, M. Zheng, W. Lv, J. Jian, X. Zhao, and C. Hu, "Physics-informed deep neural network reconstruction framework for propagation-based x ray phase-contrast computed tomography with sparse-view projections," *Opt. Lett.*, vol. 47, no. 16, pp. 4259–4262, Aug. 2022.
- [33] X. Wu, Z. Wu, S. C. Shanmugavel, H. Z. Yu, and Y. Zhu, "Physics-informed neural network for phase imaging based on transport of intensity equation," *Opt. Express*, vol. 30, no. 24, pp. 43398–43416, Nov. 2022.
- [34] S. Z. Li, M. G. French, K. M. Pavlov, and H. T. Li, "Shallow U-Net deep learning approach for phase retrieval in propagation-based phase-contrast Imaging," in *Developments in X-Ray Tomography XIV*, B. Müller and G. Wang, Eds., vol. 12242, International Society for Optics and Photonics. SPIE, 2022, p. 122421Q.
- [35] K. A. Mohan, D. Y. Parkinson, and J. A. Cuadra, "Constrained Non-Linear Phase Retrieval for Single Distance X-ray Phase Contrast Tomography," *Electronic Imaging*, vol. 2020, no. 14, pp. 146–146–8, Jan. 2020.
- [36] N. L. Johnson, A. W. Kemp, and S. Kotz, *Univariate discrete distributions*. John Wiley & Sons, 2005, vol. 444.
- [37] A. Paszke, S. Gross, F. Massa, A. Lerer, J. Bradbury, G. Chanan, T. Killeen, Z. Lin, N. Gimelshein, L. Antiga, A. Desmaison, A. Kopf, E. Yang, Z. DeVito, M. Raison, A. Tejani, S. Chilamkurthy, B. Steiner, L. Fang, J. Bai, and S. Chintala, "Pytorch: An imperative style, high-performance deep learning library," in *Advances in Neural Information Processing Systems 32*. Curran Associates, Inc., 2019, pp. 8024–8035.
- [38] D. C. Liu and J. Nocedal, "On the limited memory bfgs method for large scale optimization," *Mathematical programming*, vol. 45, no. 1-3, pp. 503–528, 1989.
- [39] J. Nocedal, "Updating quasi-newton matrices with limited storage," *Mathematics of computation*, vol. 35, no. 151, pp. 773–782, 1980.
- [40] H.-J. M. Shi and D. Mudigere, "PyTorch-LBFGS: A PyTorch implementation of L-BFGS," <https://github.com/hjmshi/PyTorch-LBFGS>, 2018.
- [41] C. R. Harris, K. J. Millman, S. J. van der Walt, R. Gommers, P. Virtanen, D. Cournapeau, E. Wieser, J. Taylor, S. Berg, N. J. Smith, R. Kern, M. Picus, S. Hoyer, M. H. van Kerkwijk, M. Brett, A. Haldane, J. F. del Río, M. Wiebe, P. Peterson, P. Gérard-Marchant, K. Sheppard, T. Reddy, W. Weckesser, H. Abbasi, C. Gohlke, and T. E. Oliphant, "Array programming with NumPy," *Nature*, vol. 585, no. 7825, pp. 357–362, Sep. 2020.
- [42] M. A. Herráez, D. R. Burton, M. J. Lalor, and M. A. Gdeisat, "Fast two-dimensional phase-unwrapping algorithm based on sorting by reliability following a noncontinuous path," *Applied Optics*, vol. 41, no. 35, p. 7437, Dec. 2002.
- [43] S. van der Walt, J. L. Schönberger, J. Nunez-Iglesias, F. Boulogne, J. D. Warner, N. Yager, E. Gouillart, T. Yu, and the scikit-image contributors, "scikit-image: image processing in Python," *PeerJ*, vol. 2, p. e453, 6 2014.
- [44] K. A. Mohan, S. V. Venkatakrishnan, J. W. Gibbs, E. B. Gulsoy, X. Xiao, M. De Graef, P. W. Voorhees, and C. A. Bouman, "TIMBIR: A Method for Time-Space Reconstruction From Interlaced Views," *IEEE Transactions on Computational Imaging*, vol. 1, no. 2, pp. 96–111, Jun. 2015.

Multi-distance Phase-Retrieval (PR) followed by FBP Reconstruction of the Multi-Material Object

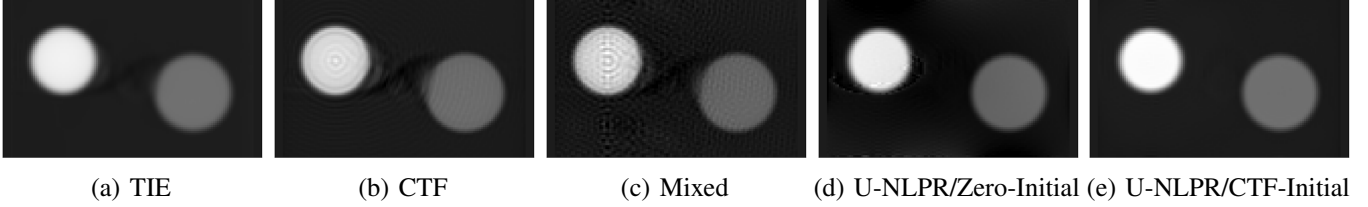


Fig. S1. Tomographic reconstructions of the refractive index decrement from the phase images produced by the CTF, TIE, Mixed, and U-NLPR (proposed) phase-retrieval (PR) algorithms. (a-e) show planar slices along the $u-w$ axes that pass through the center of the reconstruction volume. (a), (b), and (c) are using the TIE, CTF, and Mixed PR algorithms respectively. For the conventional PR methods of TIE, CTF, and Mixed, we present the best performing reconstruction with the highest SSIM (from Fig. 3). (d) shows the reconstruction using U-NLPR that is initialized with zeros for the phase and absorption. (e) shows the reconstruction using U-NLPR that is initialized with CTF at the fixed regularization in equation (17). The gray values in (a-j) are scaled between -2.53×10^{-7} and 2.03×10^{-6} . Compared to the conventional PR reconstructions in (a-c), U-NLPR reduces artifacts and noise as shown in (d, e).

Single Distance PR + FBP of Single-Material Object

Single Distance PR + FBP of Multi-Materials

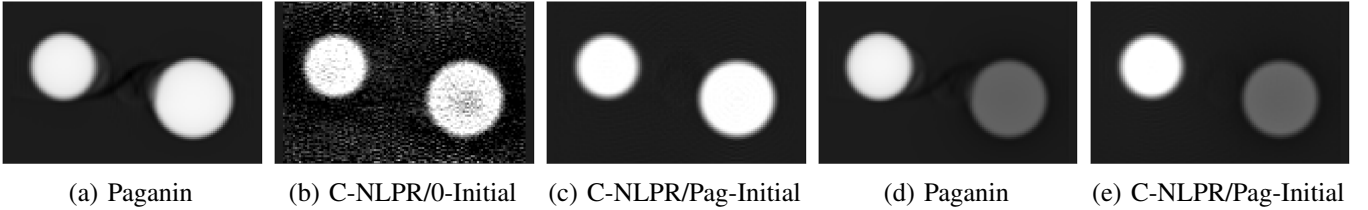


Fig. S2. Tomographic reconstructions of the refractive index decrement from the phase images produced by the single-distance phase-retrieval (PR) algorithms of Paganin and C-NLPR (proposed). (a-c) show reconstructions of the single material object. (d, e) show reconstructions of the multi-material object. (a-e) show planar slices along the $u-w$ axes that pass through the center of the reconstruction volume. (a) and (d) show reconstructions using Paganin PR. (b) shows the reconstruction using C-NLPR that is initialized with zeros for the phase image (label C-NLPR/0-Initial). (c) and (e) show reconstructions using C-NLPR that is initialized using Paganin PR (label C-NLPR/Pag-Initial). The gray values in (a-j) are scaled between -2.09×10^{-7} and 1.67×10^{-6} . C-NLPR with Paganin initialization produces the best reconstruction that minimize noise and artifacts.

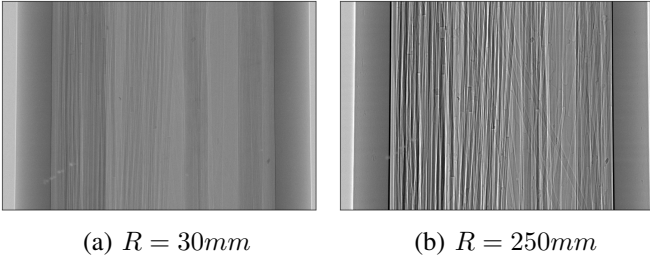


Fig. S3. Normalized X-ray images at the first view angle from synchrotron phase-contrast CT of Al , Al_2O_3 , PP , and PET fibers. (a) and (b) show the X-ray images at propagation distances of $30mm$ and $250mm$ respectively. The intensity range for the gray-values is between 0.4 and 1.2. Phase-contrast fringes are stronger in (b) than in (a) due to the larger propagation distance of (b).

VIII. QUANTITATIVE ANALYSIS OF MULTI-DISTANCE PHASE-RETRIEVAL FOR SECTION VI-B

For quantitative analysis of the reconstructions, we compare the normalized root mean squared error (NRMSE) for Al and PET fibers in Fig. S4. The NRMSE is computed only using the reconstructed values in the regions within the Al and PET fibers shown in Fig. S4 that also exclude the edges of each fiber. Importantly, to facilitate comparison with the theoretical values, we use background subtraction for the reconstructed values as explained in section V-B. From the dashed plots in Fig. S4, we can see that choosing a suitable regularization for the conventional phase-retrieval methods is challenging due to the narrow range of parameters with best performance. As the

regularization for CTF phase-retrieval is reduced, the NRMSE also reduces. For very low regularization values, all the conventional phase-retrieval methods see a moderate to large increase in NRMSE. Compared to other conventional methods, CTF results in the lowest NRMSE at the lowest regularization parameters. Hence, we still use equation (17) to secure the best performance from CTF without any manual regularization parameter tuning. U-NLPR with zero initialization for the phase results in an NRMSE that is lower than all conventional methods. However, U-NLPR with CTF initialization provides slightly lower NRMSE than U-NLPR with zero-initialization.

IX. QUANTITATIVE ANALYSIS OF SINGLE-DISTANCE PHASE-RETRIEVAL FOR SECTION VI-B

The sharpness improvement using C-NLPR/One- α is also reflected in the modulation transfer function (MTF) plot shown in Fig. S6 (a). From the MTF plot, we do not see a sharpness benefit to using C-NLPR/TrOpt- α, γ when compared to C-NLPR/One- α . The convergence speed of C-NLPR/One- α is similar to C-NLPR/TrOpt- α, γ from Fig. S6 (b). While C-NLPR/One- γ converges faster, it does not improve the sharpness as evidenced in Fig. S6 (a). Hence, C-NLPR/One- α is our choice for the C-NLPR reconstructions in Fig. 9 since it only uses knowledge of the ratio δ/β .

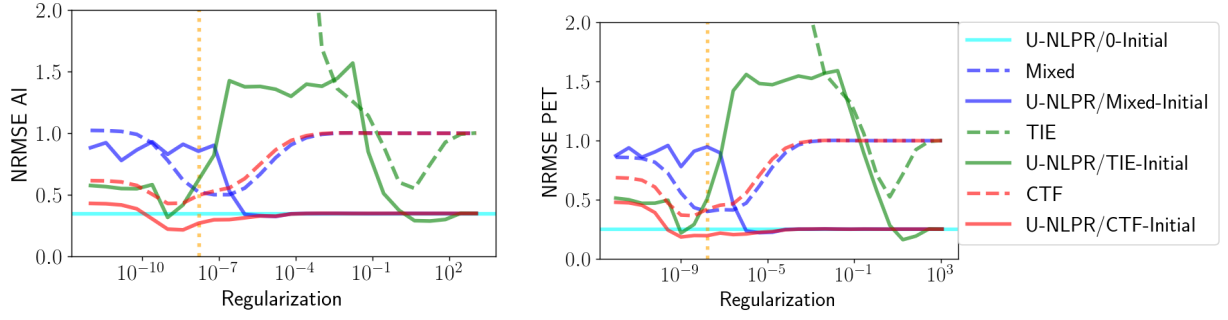


Fig. S4. NRMSE for AI and PET fibers vs. regularization of conventional PR methods. The dashed lines show the NRMSE for the conventional PR methods of TIE, CTF, and Mixed. The solid lines are the NRMSE plots for U-NLPR that is initialized using one of the conventional PR methods. While U-NLPR does not use regularization, its performance nevertheless varies with the regularization parameter of the conventional PR used for initialization. U-NLPR out-performs all the conventional PR methods irrespective of the initialization. U-NLPR with CTF initialization (regularization from equation (17) indicated by the dotted vertical orange line) has the best performance without the need for parameter tuning.

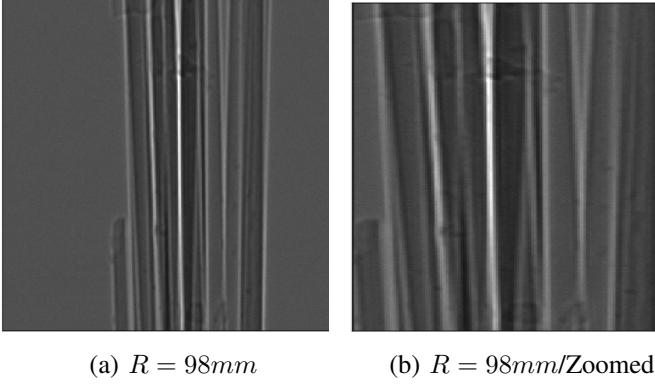


Fig. S5. (a) is the X-ray image of SiC fibers at the first tomographic view and propagation distance of $R = 98mm$. (b) zooms into the image in (a) to better visualize the phase-contrast fringes. The intensity range of gray-values is between 0.53 and 1.97.

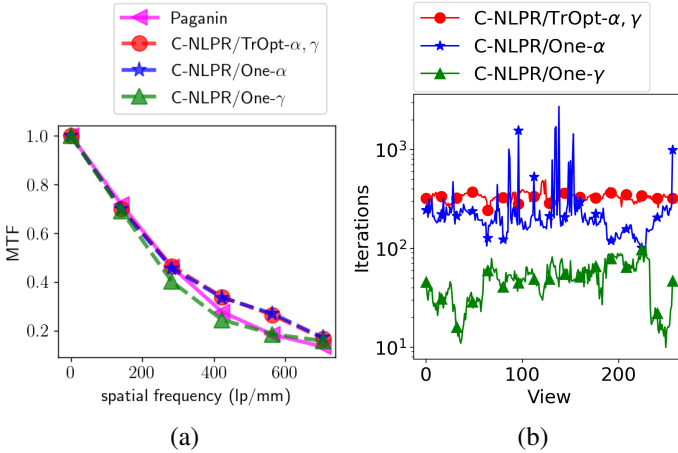


Fig. S6. (a) is a measure of sharpness using the modulation transfer function (MTF) for various single-distance PR methods. The MTF is computed for the two circles inside the red box in Fig. 9 (a, b). C-NLPR/One- α and C-NLPR/TrOpt- α, γ has a higher MTF curve than Paganin and C-NLPR/One- γ , which indicates sharper reconstructions. (b) is the number of LBFGS iterations as a function of the view index. C-NLPR/One- γ uses fewer iterations, but also suffers from lower sharpness (from (a)). C-NLPR/One- α and C-NLPR/TrOpt- α, γ use similar number of iterations for convergence.